High-resolution noncontact charge-density mapping of endocardial activation

Andrew Grace,[1,2] Stephan Willems,[3] Christian Meyer,[3] Atul Verma,[4] Patrick Heck,[1] Min Zhu,[5] Xinwei Shi,[5] Derrick Chou,[5] Lam Dang,[6] Christoph Scharf,[6] Günter Scharf,[7] and Graydon Beatty[5]

[1]Royal Papworth Hospital Foundation Trust, Cambridge University Health Partners, Cambridge, United Kingdom. [2]Department of Biochemistry, University of Cambridge, Cambridge, United Kingdom. [3]University Heart Center, University Hospital, Hamburg-Eppendorf, Hamburg, Germany. [4]Southlake Regional Health Center, Newmarket, University of Toronto, Ontario, Canada. [5]Acutus Medical Inc., Carlsbad, California, USA. [6]Cardiovascular Center, Klinik im Park, Zürich, Switzerland. [7]Physics Institute, University of Zurich, Zurich, Switzerland.

BACKGROUND. Spatial resolution in cardiac activation maps based on voltage measurement is limited by far-field interference. Precise characterization of electrical sources would resolve this limitation; however, practical charge-based cardiac mapping has not been achieved.

METHODS. A prototype algorithm, developed from first principles of electrostatic field theory, derives charge density (CD) as a spatial representation of the true sources of the cardiac field. The algorithm processes multiple, simultaneous, noncontact voltage measurements within the cardiac chamber to inversely derive the global distribution of CD sources across the endocardial surface.

RESULTS. Comparison of CD to an established computer-simulated model of atrial conduction demonstrated feasibility in terms of spatial, temporal, and morphologic metrics. Inverse reconstruction matched simulation with median spatial errors of 1.73 mm and 2.41 mm for CD and voltage, respectively. Median temporal error was less than 0.96 ms and morphologic correlation was greater than 0.90 for both CD and voltage. Activation patterns observed in human atrial flutter reproduced those established through contact maps, with a 4-fold improvement in resolution noted for CD over voltage. Global activation maps (charge density–based) are reported in atrial fibrillation with confirmed reduction of far-field interference. Arrhythmia cycle-length slowing and termination achieved through ablation of critical points demonstrated in the maps indicates both mechanistic and pathophysiological relevance.

CONCLUSION. Global maps of cardiac activation based on CD enable classification of conduction patterns and localized nonpulmonary vein therapeutic targets in atrial fibrillation. The measurement capabilities of the approach have roles spanning deep phenotyping to therapeutic application.

TRIAL REGISTRATION. ClinicalTrials.gov NCT01875614.

FUNDING. The National Institute for Health Research (NIHR) Translational Research Program at Royal Papworth Hospital and Acutus Medical.

Role of funding source: Acutus Medical provided support for the study. The opinions, interpretations, conclusions, and recommendations presented here are those of the authors and are not necessarily endorsed or representative of the views of Acutus Medical.

Conflict of interest: GB is Chief Technology Officer, MZ is Principal Scientist, XS is Senior Principal Scientist, and DC is Senior Technical Fellow at Acutus Medical and each holds stock options. LD is co-founder and holds stock and CS is a co-founder of Acutus Medical with an equity interest. The work described in this study is protected by US Patents 7,841,986; 8,417,313; 8,512,255; 8,700,119; 8,918,158; 9,167,982; 9,192,318; 9,308,350; 9,504,395; 9,610,024; 9,757,044; 9,789,286; and D782,686. Additional patents are pending in the US and worldwide.

Copyright: © 2019 American Society for Clinical Investigation

Submitted: November 30, 2018
Accepted: February 11, 2019
Published: March 21, 2019.

Reference information: JCI Insight. 2019;4(6):e126422. https://doi.org/10.1172/jci.insight.126422.

Introduction

The study of electric fields has been central to understanding the normal heartbeat (1–4) and has underpinned clinical cardiology through interpretation of surface electrocardiograms (ECGs) (5–8). The clinical discipline of cardiac electrophysiology has relied on recording and mapping intracardiac electrograms (EGMs) to identify targets for interventional therapy (9, 10). Although direct recordings from the heart allow for characterization and treatment of stable cardiac arrhythmias, unstable arrhythmias, like atrial or ventricular fibrillation, remain problematic (11, 12). Mapping such irregular rhythms requires simultaneous high-resolution interrogation of the entire heart chamber, which is technically challenging in humans (13). Our lack of understanding of mechanisms in these arrhythmias has led to largely empirical ablation strategies that are often ineffective (11, 14, 15).

Variable human anatomy is one major barrier to endocardial mapping. Stable, contiguous, nonperturbing contact with the heart muscle wall, even with multipolar basket catheters, imposes limitations in spatial resolution to the extent that interpolation algorithms have been required to gain panoramic views (16, 17). Noncontact unipolar multi-electrode arrays deployed in the cardiac chambers have helped in global, single-beat analysis of some stable cardiac rhythms (18) but technical challenges have limited their use in more complex, unstable rhythms (19). In all of these approaches, the spatially averaged nature of the cardiac electric field that arises from the whole heart becomes a smoothed distribution of potentials for which both near and distant electrical sources obscure true, local patterns of activation (4, 20).

Our aim has been to localize the compact dipolar sources of charge responsible for generating the cardiac electric field and provide a sharper, narrower view of endocardial activation achieved through a reduction of far-field interference (Figure 1). The approach is based on first principles in electrostatic field theory using physically defined quantities and providing a model-independent description of cardiac electrical activity (4, 21, 22). We report how charge density (CD), $d(\vec{y})$ at any point, can be derived from the potential $V(\vec{x})$ measured across a plurality of points distributed within a heart chamber (Figure 1A) using an inverse algorithm. Although the inverse approach is mathematically ill-posed (23), the problem has been solved by applying defined physiological constraints and numerical techniques, including regularization (4). Feasibility of the approach has first been evaluated in an anatomically realistic and clinically relevant simulation of atrial activation (24).

To resolve complex patterns of activation in the human heart, the construction of a combined imaging and multi-electrode mapping system (AcQMap) was required. Atrial anatomy was generated by ultrasonic imaging and the global distribution of CD across the anatomy was derived through the inverse algorithm from multiple, simultaneous, noncontact, unipolar EGMs. Clinical utility of the system was first demonstrated during organized atrial flutter (25–27) and secondarily in atrial fibrillation (AF). Reduction in far-field interference was confirmed in these maps and enabled identification of underlying organization amid remarkable heterogeneity. CD-based mapping provides a platform for understanding disease mechanisms and identifying clinically relevant and effective targets for ablation therapy (13).

Results

CD determination in a realistic model of atrial cardiac wavefront propagation. To evaluate the feasibility of the prototype inverse algorithm, a biophysically accurate, clinically relevant mathematical model of cardiac CD was examined using the established, open-source Chaste (Cancer, Heart and Soft Tissue Environment) platform (24). Chaste allows for simulation and analysis of the propagation of activation wavefronts within cardiac tissue by solving a set of reaction-diffusion equations. This formulation is faithful to the known principles of cellular electrophysiology and integrates contributions of membrane currents from different types of ion channels (24). As such, intracellular transmembrane action potentials and the corresponding magnitudes of extracellular CD and voltage can be accurately simulated at any location and at any instant of time.

In our simulation, the mono-domain model was used for its high computational efficiency and clinically realistic performance in modeling propagation of atrial activation wavefronts from which corresponding potentials $V(x)$ can be calculated. Chaste was employed to simulate propagation of focal activation (such as sinus rhythm, ectopy, or pacing) by injecting a stimulation current at one vertex on the chamber mesh and calculating propagation of action potentials, CD, and voltage across the chamber surface (24). For this initial evaluation of feasibility, conduction velocity was assumed to be homogeneous across the whole chamber, with a value of approximately 1 m/s (28).

The procedure to evaluate accuracy of the prototype CD inverse algorithm consisted of 4 steps, schematically depicted in Figure 2. In step 1, 30 unique wavefront propagation patterns were generated using the mono-domain model. In step 2, the distributions of CD associated with each of the propagation patterns were derived from the output of each simulation. CD is embodied as an extracellular double layer of positive and negative (dipolar) charges that electrically represent the location of the entire wavefront on the cardiac chamber surface (S) and is proportional to the spatial gradient of the transmembrane potential generated in step 1. As extracellular morphology is intrinsically different from intracellular morphology, values across these 2 domains cannot be directly compared for evaluation of accuracy. Accordingly, the gradient-derived distributions of CD established an extracellular

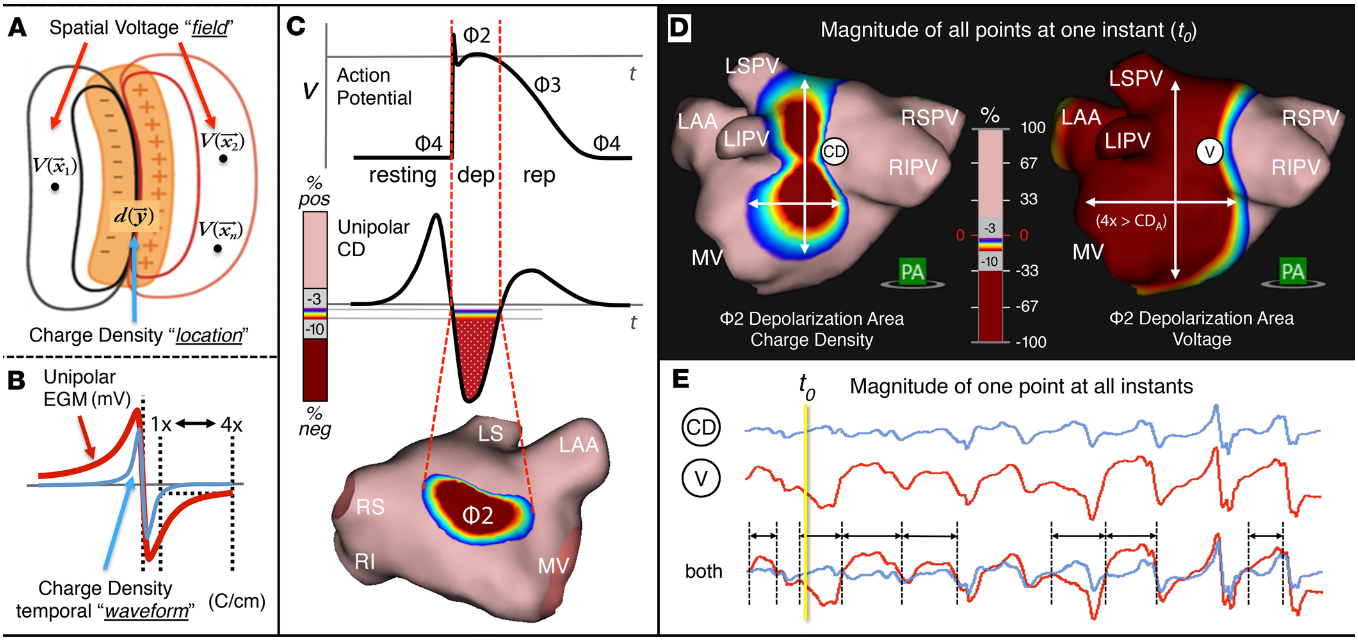

Figure 1. Spatiotemporal relationships among charge density, voltage, and action potential. (**A**) The cardiac voltage field arises as a spatially broad summation of local, dipolar charge sources generated by the action of cellular ion channels throughout the myocardium. Charge density (CD; coulombs/cm) represents the magnitude of these sources with reduced contribution from far-field sources. (**B**) Depiction of a CD waveform overlaid on a corresponding voltage-based EGM that represents the sharper, narrower nature of CD and a 4-fold improvement in temporal resolution over voltage. (**C**) Area of depolarization shown on a CD map at a specific instant of time, with the red region depicting the associated negative phase of CD. The area-spanning space is correlated with the temporal duration of the negative phase of the CD waveform and with phase 2 of the action potential. (**D**) Spatial distribution of depolarization area for a CD map displayed beside the corresponding voltage-based map that demonstrates a 4-fold improvement in spatial resolution of CD over voltage. Spatial maps display the magnitude of all points at one fiducial instant of time (t_0) corresponding to the yellow time cursor in the waveform in panel **E**. Propagation is ascertained by animation of the maps from each sample instant through time. PA, posterior-anterior. (**E**) Temporal CD waveform overlaid on the corresponding voltage-based waveform that demonstrates an average 4-fold improvement in temporal resolution of CD over voltage. Temporal waveforms display the magnitude of one point at all instants of time. The lower-magnitude, fractionated morphology represents localized irregular activation (LIA; see Figure 6A), which is the dominant conduction pattern in AF and for which the resolution of CD is improved the most over voltage. The larger-magnitude, organized morphology represents localized rotational activation (LRA; see Figure 6A), which is a nondominant, regionally organized conduction pattern in AF and for which the resolution of CD is improved over voltage, but less so than noted for LIA. LIPV, LSPV, RIPV, RSPV are left and right inferior and superior pulmonary veins, respectively; MV, mitral valve.

foundation of a priori known values from which ground-truth potentials and activation times were forward calculated and compared with inverse-reconstructed potentials and activation times, with all such values determined on the chamber surface.

In step 3, the set of inverse-reconstructed distributions of CD associated with the set of ground-truth potentials calculated in step 2 were derived using the prototype CD inverse algorithm. The *x-y-z* coordinates of the chamber surface vertices and nominal electrode positions were applied as input to the algorithm, together with the 48 ground-truth potentials for every time instant. From the inverse-reconstructed distributions of CD, forward-reconstructed potentials were forward calculated and activation times were postprocessed across the chamber surface. In step 4, the CD inverse algorithm was evaluated by comparing the forward-reconstructed chamber-surface potential distributions and activation times (from step 3) with the ground-truth chamber-surface potential distributions and activation times (from step 2).

Realistic surface meshes of both the right atrium (RA, 52 × 57 × 59 mm) and the left atrium (LA, 71 × 46 × 57 mm) were segmented from CT scans of a single human male subject. The surfaces were tessellated into high-density triangular meshes (RA: 8,818 vertices, 17,530 triangles; LA: 8,864 vertices, 17,580 triangles) to represent the endocardial surface of each atrial chamber (29). Thirty sites (15 RA, 15 LA) were selected from broadly distributed locations to simulate focal activation. The work flows contained within each of the steps listed above are charted in Figure 2 and were carried out for each of the simulated sites of focal activation and evaluation (see detailed description in supplemental materials; supplemental material available online with this article; https://doi.org/10.1172/jci.insight.126422DS1).

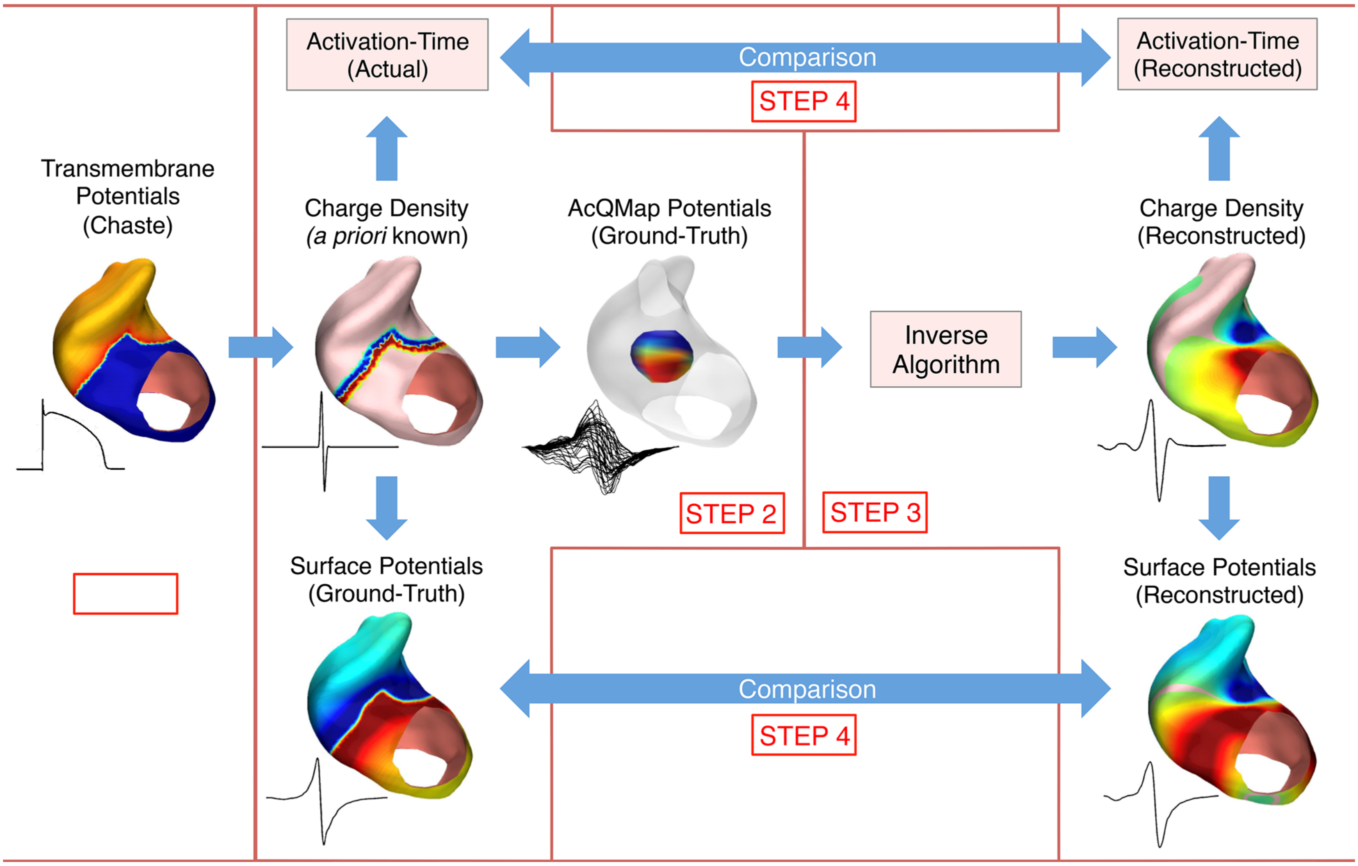

Figure 2. Four computational steps were completed to evaluate the accuracy of the CD inverse algorithm in a biologically realistic simulation. Step 1 is simulation of action potential propagation. Step 2 is calculation of a priori known CD, ground-truth potentials, and actual activation times. Step 3 is inverse reconstruction of CD, forward reconstruction of potentials, and postprocessed activation times. Step 4 is comparative evaluation of forward-reconstructed potentials and activation times with ground-truth potentials and activation times.

The accuracy of reconstructed CD and voltage was evaluated (Supplemental Figure 1) from 4 key aspects: (a) similarity of voltage waveform morphology and timing, (b) similarity of the spatial path of propagation over the duration of propagation, (c) correspondence between activation times of CD and voltage, and (d) spatial accuracy in localization of focal sites of activation. Cross-correlation and correlation time difference (Xcorr and Tdiff; applied to ‘a’), area under the receiver operating characteristic curve (AURC; applied to ‘b’ and ‘c’), and distance between the site of early activation and the true origin of activation (D2O; applied to ‘d’) were adopted as evaluation metrics (see supplemental materials for further details). Clinically practical acceptance criteria were applied to the results, with thresholds defined as:

Spatial error < 5 mm (90% confidence)
Temporal error < 6 ms (90% confidence)
Morphologic correlation > 0.7 (90% confidence)

These criteria have been established in the literature (18, 19, 30) and are derived from the practical requirement to deliver a single clinically relevant ablation lesion (5-mm diameter) to a specific target using an electrode catheter. The results of all evaluations are listed in Table 1.

Accuracy of forward-reconstructed voltage versus ground-truth voltage. Cross-correlation was performed on a total of 6,000 pairs of voltage waveforms (200 comparison points from 30 simulations of focal propagation) (Supplemental Figure 2). The distributions of Xcorr and Tdiff comparing forward-reconstructed voltage waveforms versus ground-truth voltage waveforms, respectively, are summarized in Figure 3, A and B. Xcorr demonstrated a median value of 0.895, with 90% of correlation values greater than 0.7 (Figure 3A). Tdiff demonstrated a median value of 0.960 ms, with 90% of time-shift values of 6 ms or less (Figure 3B). Because time-shift values were biased toward zero, a nonparametric method was performed to calculate the confidence interval (1-sided) for a 90% tolerance interval over 90% of the population.

Table 1 shows confidence greater than 90% at a level equal to the minimum acceptable correlation of 0.7 for Xcorr (lower bound = 0.702) and below the maximum acceptable time shift of 6 ms for Tdiff (upper bound = 4.800 ms) (Table 1).

Spatiotemporal accuracy of the activation sequence. AURCs of propagation history maps (20-ms window) were calculated for a total of 3,929 time frames over 30 focal simulations (Supplemental Figure 3). Figure 3C summarizes distributions of AURCs comparing (a) activation times for inverse-reconstructed CD versus actual activation times (CD versus Sim), and (b) activation times for forward-reconstructed voltage versus actual activation times (Voltage versus Sim). CD demonstrated the same median AURC value as voltage (0.908 versus 0.907, respectively), but a tighter interquartile range (IQR = 0.892–0.922 versus 0.884–0.925, respectively). Consequently, CD was significantly better than voltage in estimating activation time (*t* test, $P < 0.0001$; Mann-Whitney test, $P < 0.003$). Confidence was also calculated on each AURC distribution using a 1-sided nonparametric test for a 90% tolerance interval over 90% of the population (Table 1). Both CD and voltage had confidence greater than 90%, again well above the minimum acceptable confidence interval of 0.7 (Table 1).

Spatiotemporal correspondence between CD and voltage. Figure 3D summarizes distributions of AURCs of propagation history maps (20-ms window) over 30 focal simulations comparing activation times for inverse-reconstructed CD versus activation times for forward-reconstructed voltage (see also Supplemental Figure 4). A high correspondence is demonstrated with a narrow range of variation (median = 0.917, IRQ = 0.899–0.934). Confidence was also calculated using a 1-sided nonparametric test for a 90% tolerance interval over 90% of the population. Confidence was greater than 90%, well above the minimum acceptable confidence interval of 0.7 (Table 1).

Spatial accuracy of the site of focal origin. D2Os were also calculated for 30 focal simulations. The simulated foci were broadly distributed across the RA and LA, with 15 sites located in each chamber (Supplemental Figure 5). Figure 3E summarizes distributions of D2Os for inverse-reconstructed CD and forward-reconstructed voltage. The median value of D2Os obtained from CD was 28% smaller than those obtained from voltage (1.725 versus 2.410 mm) and had 64% less interquartile variation (IQR = 1.250–2.461 versus 1.503–4.867 mm). Twenty-seven out of 30 CD D2Os (90%) were less than 5 mm, compared with 25 out of 30 voltage D2Os (83%). Mann-Whitney test indicated that CD was more accurate in localizing the site of focal origin than voltage ($P < 0.08$) (Table 1). Importantly, CD with its inherent spatial specificity is the default mode of the clinical mapping system on which all modes of diagnostic map displays are based (Figure 1).

Intracardiac ultrasound provides accurate reconstruction of endocardial anatomy. Simulation models do not completely reproduce the behavior of complex human arrhythmias, which limits the weight of their results on translational interpretation (13, 31). In addition, no gold standard comparator for CD presently exists in an animal model (4). Accordingly, overall feasibility was next tested directly in vivo in human atria. High-resolution ultrasound was incorporated as a central feature in a catheter designed to localize the endocardial surface of atrial chambers and provide a clinical platform for inverse solutions and CD calculation (Figure 4, A–C). Endocardial surfaces were algorithmically reconstructed from the ultrasound point set acquired by the catheter in both right and left atria (Figure 4D and Supplemental Video 1). Nine patients (56% male, mean age 63.3 ± 9.4 years with left atrial diameter 43.0 ± 7.1 mm) were enrolled with complete data sets for left atrial anatomy collected from each subject. The absolute median distance between surfaces derived from corresponding intracardiac ultrasound and prior CT measurements was 1.85 mm (IQR = 0.86–3.43 mm). Real-time ultrasound-based LA reconstruction compared favorably to surface CT images.

CD improves accuracy in mapping atrial activation. Typical atrial flutter is a well-understood arrhythmia based on a stable, cavotricuspid isthmus–dependent (CTI-dependent), macro-reentrant circuit that manifests in the RA and is readily accessible for investigation (25–27). Within the initial feasibility work in humans, AcQMap CD and voltage-based maps were compared with those obtained from an existing commercial contact-based 3D mapping system (26). Six patients were mapped with both AcQMap and the commercial system. The patient group had a history of persistent AF and atrial flutter, with prior ablations performed in 3 of the 6 patients. Enlarged left atria (≥45 mm) were noted in all patients, with 3 right- and 5 left-sided flutters mapped. The average flutter-cycle length was 275 ± 75 ms with a range of 206–445 ms. Noncontact and contact voltage–based activation maps demonstrated the same macro-reentrant conduction pattern in terms of activation time and direction. Figure 5 and Supplemental Video 3 present an example of a typical, counter-clockwise flutter

Table 1. Summary of AcQMap performance with statistical summary of evaluation metrics

Map Accuracy Category	Evaluation Metric	Results		Confidence Interval	Confidence
		Mean ± SD	Median (IQR)		
Voltage vs. Simulation (Sim)	Xcorr	0.862 ± 0.111	0.895 (0.805–0.945)	Lower 0.702	90.2%
	Tdiff (ms)	2.045 ± 2.894	0.960, (0.320–2.560)	Upper 4.800	90.2%
	AURC	0.902 ± 0.031	0.907 (0.884–0.925)	Lower 0.857	90.2%
	D20 (mm)	2.972 ± 1.898	2.410 (1.503–4.867)	NA	NA
CD vs. Simulation (Sim)	AURC	0.906 ± 0.023	0.908 (0.892–0.922)	Lower 0.876	90.2%
	D20 (mm)	2.228 ± 1.633	1.725 (1.250–2.461)	NA	NA
CD vs. Voltage	AURC	0.913 ± 0.031	0.917 (0.899–0.934)	Lower 0.877	90.2%

Confidence intervals were calculated using 1-sided nonparametric test with a 90% tolerance interval over 90% of the population. Confidence test was not performed over the D20 data because of the small number of data samples. The small variations among the 30 data points suggest the number of samples is acceptable in this evaluation.

in the RA. In Figure 5, the propagation-history color bands are set to display an activation map of the entire cycle length, shown in anterior-posterior (AP) and left-anterior-oblique (LAO) views. The map and waveforms reveal the activation sequence progressing inferiorly from the roof on the lateral wall (LAT), medially on the isthmus (CTI), and superiorly on the septum (SEP). Waveforms sampled from 8 evenly spaced locations around the entire RA show the expected morphology and timing of propagation through the entire flutter-cycle length represented by the translucent-gray region. As shown in Figure 1C, the spatial span of the negative phase of CD, at any instant of time, correlates with the temporal duration of phase 2 of the transmembrane action potential for any point located along the leading edge of the wavefront. Accordingly, the negative phase of CD signifies the area of depolarization on the 3D map. Figure 1D shows a side-by-side image of raw CD and voltage, with the color bands set to fully display the negative phase of both CD and unipolar voltage. The area of depolarization for raw CD and voltage was calculated and compared for every map frame throughout the flutter-cycle length of all 6 patients, with voltage delineating an area 4.17 ± 1.22 times larger than CD. Temporal features of deflection in the associated waveforms show the same level of broadness in voltage, as compared with CD. This 4-fold improvement in resolution in space and sharpness in time is being further examined in a subset of patients from our prospective study in persistent AF, described below, with results to be reported separately.

CD reveals classifiable activation patterns in persistent AF. Having established the feasibility of the system to map a well-understood arrhythmia, a series of patients with persistent AF were enrolled to evaluate a complex arrhythmia that remains inadequately characterized by conventional means. Three sites enrolled 10 patients (mean age 60.1 ± 9.2 years; 93% male; AF duration 5.4 ± 4.6 years and LA diameter 44.7 ± 3.9 cm). Six of the patients were scheduled for de novo ablation and none had received recent exposure to the antiarrhythmic drug amiodarone. A total of 42 activation patterns (average fibrillatory cycle length 142 ± 25 ms) were observed at 23 sites specific to each patient and empirically classified into 1 of 3 types (Figure 6A and Supplemental Videos 4–6): (a) focal activation, with radial conduction from a single location ≥ 3 times per 5-second duration of AF, was seen in 31% of the identified patterns; (b) localized rotational activation (LRA), a regionally organized pattern of conduction that rotates in one direction around a confined zone (clockwise or counter-clockwise) and subtends a path of ≥ 270 degrees, was seen in 31%; (c) localized irregular activation (LIA), a disorganized pattern of conduction with repetitive, multidirectional, isthmus-like conduction through a small confined zone that may enter, exit, and pivot within and around the zone, was seen in 38%. Sixteen sites exhibited more than one activation pattern, with LIA being dominant and which voltage-based mapping cannot reliably discern (Supplemental Video 2). The average number of patterns per patient was 7, with the number of patterns, average cycle length, and locations illustrated (Figure 6B and Table 2).

CD identified AF activation patterns amenable to ablation that restored sinus rhythm. The ability to visualize clinically relevant targets located outside the pulmonary venous ostia prior to initiating ablation allows alteration of conventional ablation treatment strategies to incorporate these targets. One representative 70-year-old male patient with a history of highly symptomatic persistent AF had failed 5 attempts at

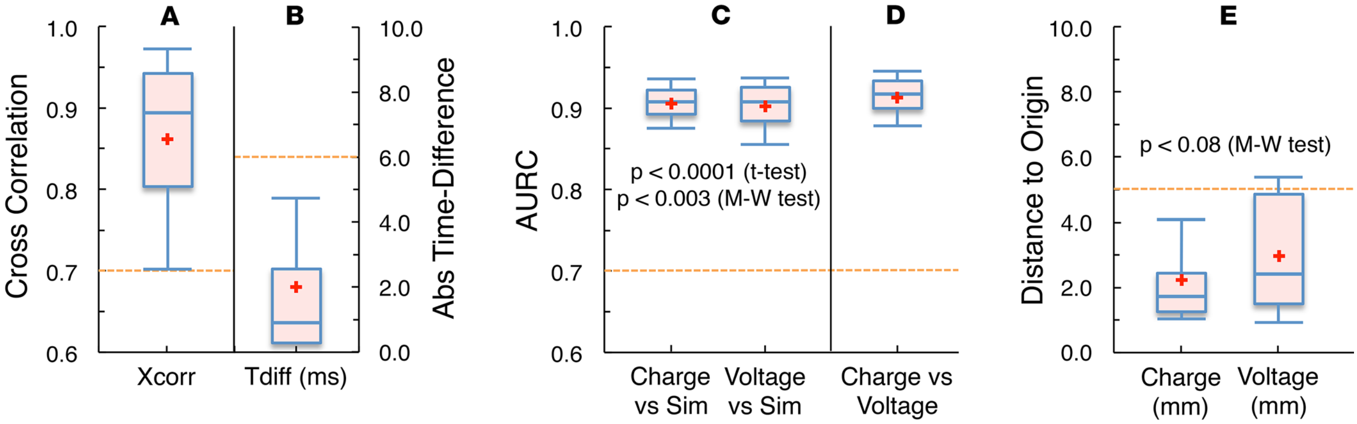

Figure 3. Performance comparisons and spatiotemporal accuracy of reconstructed CD and voltage in a biologically realistic simulation. (**A**) Box-and-whisker plot of Xcorr distribution from 6,000 pairs of voltage waveforms. (**B**) Box-and-whisker plot of Tdiff distribution from 6,000 pairs of voltage waveforms. (**C**) Box-and-whisker plot of AURC distributions from 3,929 time frames comparing spatiotemporal overlap of CD and voltage activation times versus actual activation times. Paired *t* and Mann-Whitney (M-W) tests indicated that activation times were similar ($P < 0.0001$ and $P < 0.003$, respectively). (**D**) Box-and-whisker plot of D2O distributions from 30 focal simulations. (**E**) Box-and-whisker plot of D2O distributions for inverse-reconstructed CD and forward-reconstructed voltage. CD was more accurate in localizing the site of focal origin than voltage ($P < 0.08$). In all plots, boxes span from quartiles Q1 to Q3 and whiskers span from the 10th to 90th percentiles of the population. The red cross denotes the mean value and the blue horizontal bar denotes the median value. The dashed lines delineate the minimum acceptable correlation value of 0.7, or the maximum acceptable time shift of 6 ms, or the maximum acceptable D2O of 5 mm.

electrical cardioversion over the previous 5 years. Initial maps of AF observed during CD mapping showed a single dominant LIA in the posterior view that occasionally alternated into a rotational conduction pattern through the same site (Figures 6A and 7B, and Supplemental Videos 5 and 6), the central point of which could be incorporated within a somewhat modified ablation line around the left pulmonary veins. Contiguous ablation lesions were placed down the posterior wall with an approximately 1.5-cm-wider encirclement than would be usual below the left inferior pulmonary vein to include the identified LIA (Figure 7, A and B, and Supplemental Video 7). Approximately 45 seconds after passing the ablation treatment into the core of the target, AF converted into sinus rhythm. Isolation of the right pulmonary veins was completed with subsequent noninducibility demonstrated in response to rapid atrial pacing (Figure 7C). The patient remains in normal sinus rhythm without the need for antiarrhythmic drug treatment since the procedure was performed 28 months ago.

Discussion

Here, we show through application of first principles of electrostatic field theory, that the sources of the cardiac electric field responsible for both the ECG and intracavitary voltage recordings can be resolved. Initially, the prototype algorithm for mapping cardiac electrical activity was shown to be feasible in an established, biologically realistic simulation. Next, a specialized catheter-based system was developed that provides recording of the cardiac potential field and computation of equivalent charge sources on the endocardial surface. Through application of this system in human atrial chambers, the first global, continuous maps of AF were obtained with reduction of interference from far-field sources. These maps enable greater insight into disease mechanisms and provide a platform for patient-specific treatment.

The heart's potential field results from the summation of many tiny electric dipoles that are defined as charge sources (q_+) closely coupled with equivalent sinks (q_-) (2, 6, 7, 32). These microscopic sources arise from ion channels within the membrane of myocardial cells and are understood as the origin of the macroscopic distribution of potentials that are responsible for both the intracardiac EGM and the body-surface ECG (1, 4, 6). Localizing the sources (also called equivalent generators) of bioelectric fields has long been seen as desirable (6, 33), even though the earliest theoretical studies of electric fields from nerve or muscle established that it would not be physically possible to measure such sources directly (2, 20). Consequently, sources have to be derived from observed fields (21, 34), which has proven challenging (4, 23, 35).

Source models initially evolved from a hypothetical double layer as an equivalent source at the cellular membrane (2, 6, 35, 36), with the moment of excitation in this model believed to be due to the presence of dipoles at phase boundaries (6, 37). The observed potentials then arose from the combined effects of dipole moments due to positively charged sodium ions moving across cell membranes, with negatively charged proteins and anions being held in an intracellular location (38). Such low-magnitude currents were determined to be physically localized within membrane ion channels and are directly responsible for the formation of the transmembrane action potential (39). Since the 1960s, source models have evolved to include distributions of current density that extend from all active ion channels and flow throughout the entire extracellular torso-volume. This is an ohmic model that assumes a source current as the origin of the extracellular potential field that manifests from the flow of current across the volume-conductor impedance (1, 2, 35, 36, 40). However, such a view is inconsistent with first principles of electrostatic field theory (4, 21, 22, 34, 41), which state that a distribution of current density (charge in motion) generates a magnetic field, while an electric field arises from a static (or quasi-static) distribution of CD (4, 21, 34). Accordingly, our approach to determine the sources has been based on calculating the polarization CD of active cells that represents the true physical source of the measured cardiac electric field (4). Variation in CD across space and time spreads through the tissue as a propagating wave of depolarization with algorithmic solution of the inverse problem from potential $V(\vec{x})$ to CD, $d(\vec{y})$, providing a propagation map (4). The prototype algorithm employed a distance-weighted average across space according to the microscopic Maxwell's equations (4, 34) and for which the excitation dynamics are governed by electrochemical action of ion channels (38).

Other approaches have been investigated to track broader patterns of cardiac activation as an alternative to true source calculation. For example, electrocardiographic imaging (ECGi) based on a vectorial body surface representation of the cardiac electric field (7) is the subject of experimental investigation (42–44). However, the potential field diminishes with distance from myocardial sources which, in the case of atrial signals, results in a low signal-to-noise ratio for recordings from the body surface and diffuses the images of atrial sources (3, 6, 42, 44). While the determination of the potential (the so-called forward problem) is well posed with a continuous relationship between the data and the solution, there is considerable variation between simulated and measured body surface potentials (42). The limitations of surface recordings are further compounded when inverse solutions with regularization methods are then applied to minimize the effects of small errors in data collection (measurement noise, geometry errors, inaccurate conductivity values) that would otherwise cause significant errors in the solution (42, 43). Despite these challenges, plausible source localization has been obtained, albeit with limitations in spatially distinguishing endocardial from epicardial activation (44–46).

Conventional measurements that underpin clinical cardiac electrophysiology are obtained by placing electrodes in direct contact usually with the endocardium (9, 10, 47). The catheters so employed were designed to sequentially sample single or multiple points of endocardial contact that form a panoramic map of activation, with annotation referenced to a stable time of activation at a single point. Sequential methods of mapping are intrinsically unable to annotate or determine the direction of irregular activation wavefronts required for global mapping of complex, unstable arrhythmias, such as AF. To address the identification of fibrillatory mechanisms without annotation to a reference, multipolar basket catheters (MBCs) (16) and more recently higher-density mapping electrodes (48) have been developed. Significant limitations have been reported in the resulting contact EGMs, such as interference from far-field sources, low spatial resolution, equatorial bunching, and mechanical artifacts related to motion and contact pressure (49).

Our objective of quantifying charge sources required a set of potential measurements suitably distributed across the atrial chamber cavity and sampled through time (3, 4, 33). Intracavitary recordings of EGMs were therefore acquired without direct contact with the heart wall that, both simultaneously and as a whole, represent the instantaneous activity of the entire heart chamber (global mapping). Such noncontact measurement procedures, first conducted in canines using olive-shaped or cylindrical probes (50), rely on solid-angle theory in which the potential obtained at any point by the device is seen to be proportional to the angle subtended by the full edge length of the wavefront to that point (4, 50–52). This would result in an accurate calculation only if the magnitude of CD was constant across the entire wavefront. Nonetheless, this early work demonstrated feasibility of the concept despite significant spatial variation in CD. Initial methods for obtaining noncontact recordings were refined through mathematical modeling (53) and it was observed that intracavitary potentials correlated strongly with intramural contact recordings (54). Noncontact multi-electrode

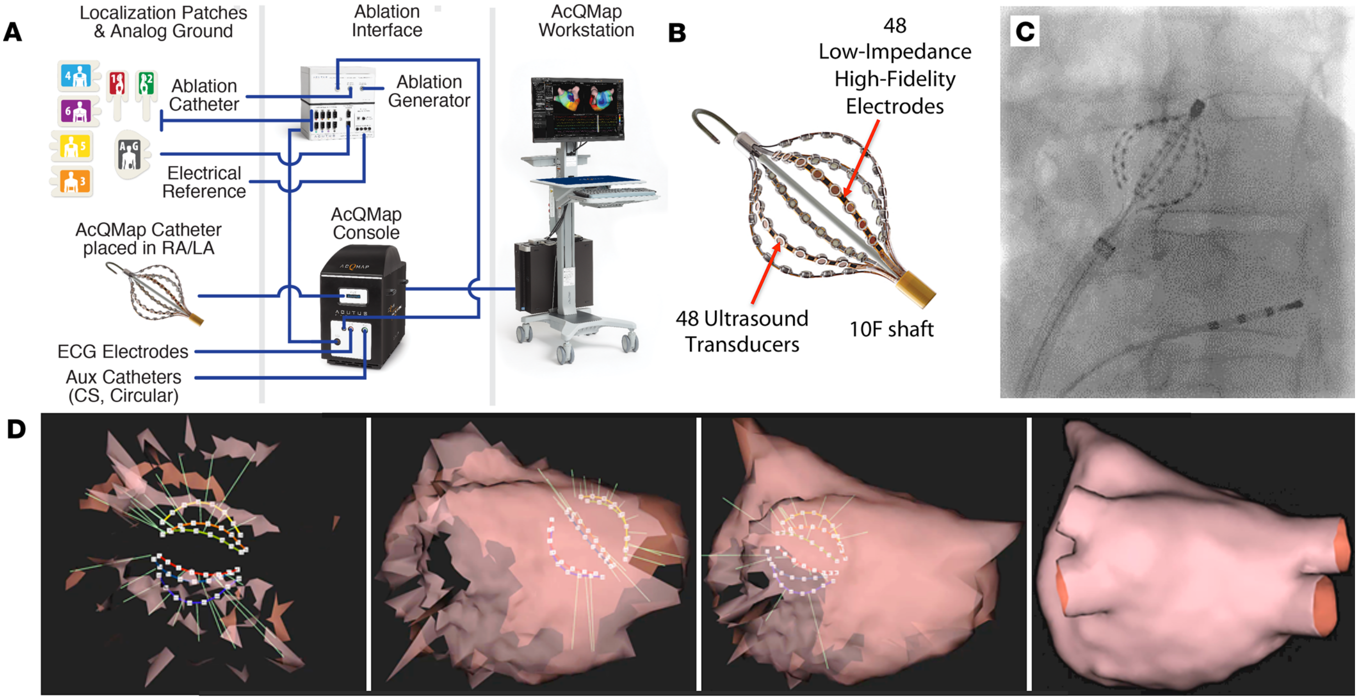

Two seconds 45 seconds 105 seconds Final post-processed anatomy

Figure 4. System, mapping catheter, and anatomic reconstruction used in clinical studies of human atria. (**A**) The system consists of a console, workstation, and interface unit. Localization and electrical reference electrodes are connected to the system through the patient interface. The AcQMap catheter, ECG electrodes, and auxiliary catheters are connected to the console front panel. Commercially available ablation catheters and generators can be connected through an ablation interface. (**B**) AcQMap mapping catheter has a 10-F shaft, integral handle (not shown), and deployable distal 25-mm spheroid apparatus that has 6 splines, each populated with 8 ultrasound transducers for anatomy reconstruction and 8 unipolar electrodes for mapping. (**C**) Radiographic (28° left anterior oblique [LAO]) view of the AcQMap catheter in the left atrium. (**D**) Ultrasound reconstruction of the left atrium is based on the transit time of sonic reflections between the endocardial surface and the transducers on the catheter splines. Distances calculated from the transit times result in 3D points that represent locations on the endocardial surface and are dynamically triangulated into a surface mesh. Rotation, advancement, and retraction of the catheter during point collection achieves a complete reconstruction throughout the entire chamber, usually over 90–180 seconds (Supplemental Video 1). Postprocessing is performed to establish the final anatomy that is used for navigation and mapping.

array balloon catheters were later engineered that provided instantaneous isopotential maps on a virtual reconstructed endocardium (51, 52), enabling use in clinical studies (18). The approach has proven valuable in research applications providing global maps of the entire endocardium (18, 19, 30). However, significant far-field interference, inaccuracy of geometry, and degradation of accuracy at distances greater than 40 mm from the center of the probe prevented the technology from becoming a routinely applied clinical tool (19, 30). To calculate CD with high fidelity, we required accurate anatomy to determine the optimum transform between the endocardial surface and the noncontact electrodes. Accordingly, high-resolution ultrasound transducers were incorporated as a central feature in the catheter design to obtain a true anatomy not reliant solely on panoramic accumulation of mapping electrode positions. The approach minimizes errors due to motion, provides accurate distance measurements, and facilitates overall system stability that, together, address many of the challenges encountered by the impedance-based approach for localizing the 3D coordinates of noncontact catheter electrodes (19).

Our simulation studies showed that the prototype inverse algorithm reconstructed chamber-surface voltages from 48 intracavitary unipolar measurements with high correspondence to the simulated ground-truth voltages. Waveform morphology correlated with a median value of 0.895 and a median time shift of 0.960 ms, which exceeded the acceptance criteria of cross-correlation greater than 0.7 and time shift of 6 ms or less. These results represent an improvement over prior studies that directly compared noncontact and contact endocardial potentials in vivo and reported a mean cross-correlation of 0.82 for sites less than 40 mm from the center of a noncontact catheter during sinus and paced rhythms (51). The prototype inverse algorithm also accurately reproduced the activation pattern across

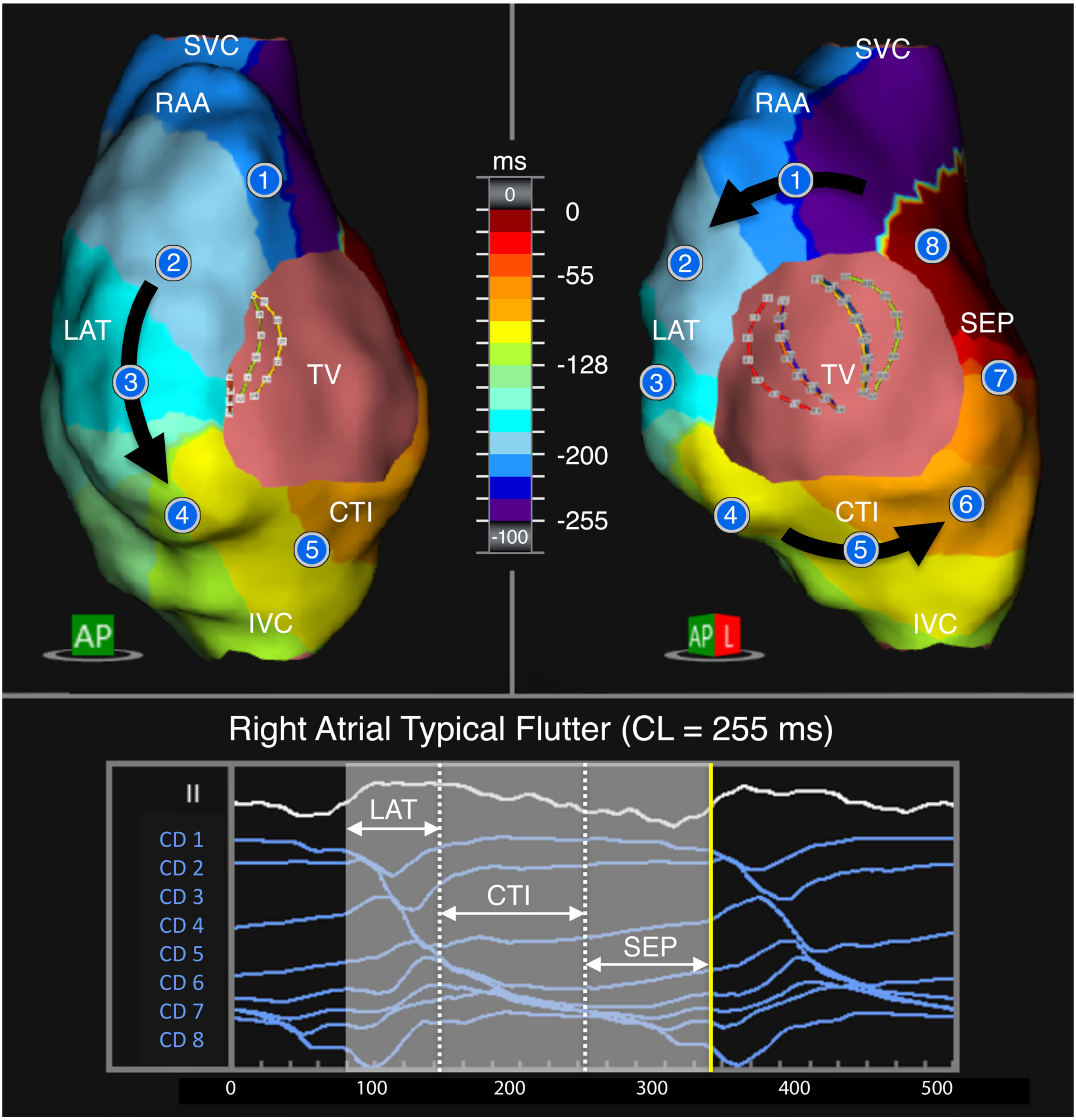

Figure 5. Initial clinical validation in typical cavotricuspid-isthmus–dependent atrial flutter. Example of typical, counter-clockwise flutter in the right atrium. In the upper panel, the propagation-history color bands are set to display a fixed propagation-history map of the entire cycle length, shown in anterior-posterior (AP) and left-anterior-oblique (LAO) views. Signals can be visualized from any position on the map (labeled on the anatomical mesh) and at any instant of time due to the global, simultaneous calculation of the inverse solution. The duration of propagation history can be adjusted by the operator and is demarcated by the translucent-gray region in the lower panel. The yellow time cursor at the right edge of the history window corresponds to the leading edge of the red color band on the map, shown reaching the roof from the septum. The other color bands, located progressively clockwise, represent the location of the wavefront at earlier instants of time. The span of the color bands, across space, and the associated duration of the translucent-gray region, across time, were set equal to the flutter-cycle length (CL, 255 ms). Accordingly, waveforms sampled from 8 evenly spaced locations around the entire right atrium reproduce the expected morphology and timing of propagation, while the map reveals the activation sequence progressing inferiorly from the roof on the lateral wall (LAT), medially on the isthmus (CTI), and superiorly on the septum (SEP). IVC, inferior vena cava; RAA, right atrial appendage; SVC, superior vena cava; TV, tricuspid valve.

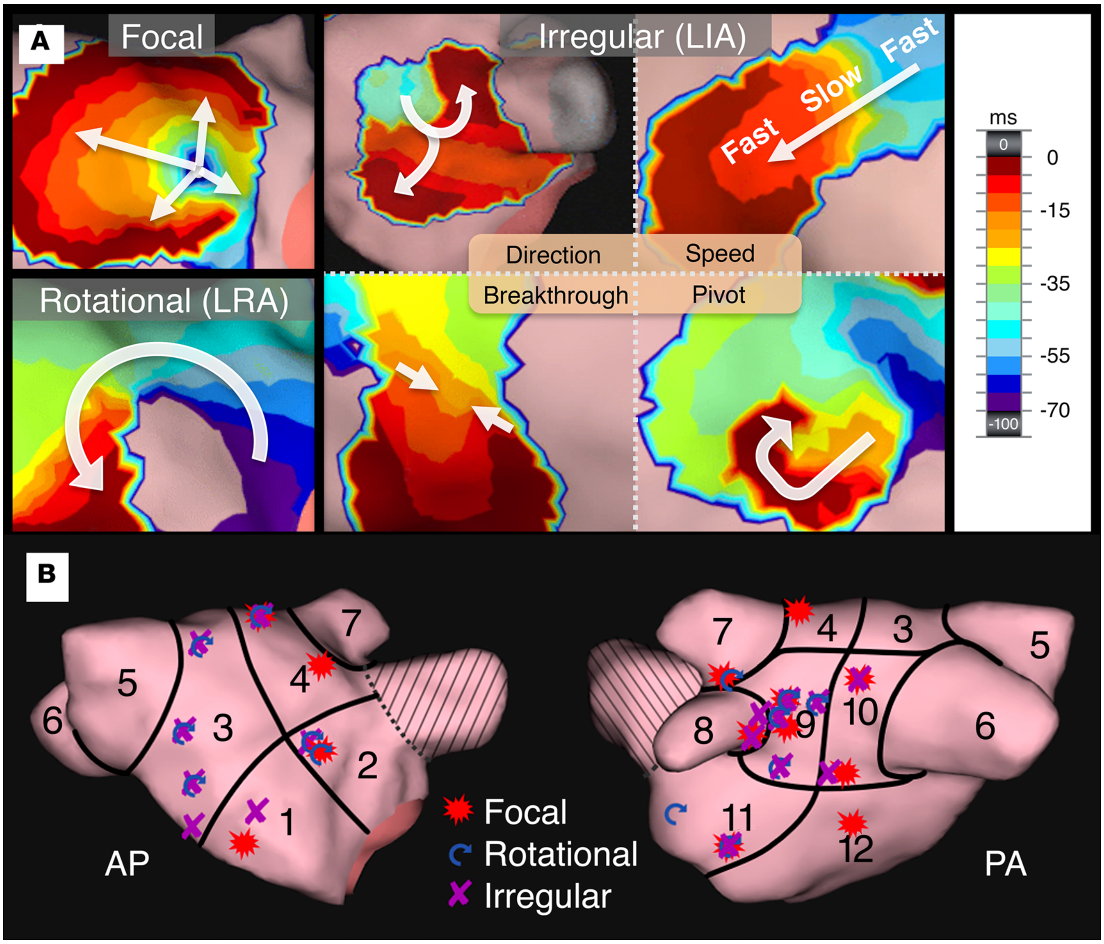

Figure 6. Conduction patterns identified in propagation history maps and localization of activation patterns of atrial fibrillation. (**A**) Three discrete identified conduction patterns, including focal activation, with radial conduction from a single location ≥ 3 times per 5-second duration of AF; localized rotational activation (LRA), with ≥ 270 degrees of conduction around a fixed, confined zone; and localized irregular activation (LIA), with repetitive, multidirectional entry, exit, and pivoting conduction through and around a fixed, confined zone (see Supplemental Videos 4–6). (**B**) Spatial plot of conduction patterns and locations identified in a subset of 10 patients recruited into the DDRAMATIC SVT trial. Conduction patterns were identified at patient-specific locations throughout the atrial body (regions 1–12), with one or more patterns arising from the same location.

the chamber surface, with a median AURC of 0.907 (Supplemental Figure 4). Comparison between activation times from inverse-reconstructed CD and activation times from forward-reconstructed voltage also revealed a high correspondence, with a median AURC of 0.917. Compared with voltage, CD had less AURC variability, indicating that the prototype CD-based inverse algorithm retained the resolution of simulated wavefronts with a high true-positive rate, but did not introduce artificial complexity to the propagation pattern. The origin of simulated focal activity can be located by the CD inverse algorithm with a median accuracy of 1.725 mm, which exceeded the acceptance criterion of 5 mm. When clinical data were acquired and applied, the algorithm provided voltage- and CD-based maps of endocardial activation during atrial flutter that reproduced prior findings obtained using both contact (26, 27, 55) and noncontact EGMs (25). The key advantage, as explicitly demonstrated in Figure 1, is that clinical CD maps and waveforms provide an average 4-fold improvement in spatial and temporal resolution, respectively, when compared with voltage. A further advantage, demonstrated in Supplemental Video 2, is that CD can reliably discern the LIA pattern, while voltage-based mapping cannot resolve this pattern, as voltage suffers from spatial blending across simultaneously distributed sources within and around these discrete sites.

AF is inherently unstable, with a constantly changing activation pattern that cannot be mapped like a stable and regular arrhythmia, such as atrial flutter (56). While intuitively viewed as being random (57), AF has in fact an underlying organization, supported experimentally (57–60), and specific

Table 2. Summary of total number of conduction patterns and average fibrillatory cycle length (CL) in each left atrial region

Patient	Focal	LRA	LIA	Average CL (ms)
1	1		1	174
2	1	2	1	137
3		3	4	136
4	3	1	1	138
5	1	1		129
6	1		2	122
7	2	4	4	116
8	2		2	168
9	1	2	1	115
10	1			183

These data are based on the same subset of 10 patients in Figure 6B. The dominant pattern was LIA, which cannot be reliably discerned with voltage-based mapping (see Supplemental Video 2).

spatiotemporal patterns that are now clinically recognized (61–64), with termination of arrhythmia in response to focal ablation (65). There are, however, continuing challenges related to spatial and temporal resolution that have generated much conflicting data and have fueled a robust debate regarding mechanisms of conduction and strategies for therapeutic intervention (13, 17, 64, 66, 67).

The CD maps obtained in this evaluation of feasibility address the current impasse and are likely to represent true maps of human AF for several reasons. First, the enhanced sensitivity and specificity of the measurements are based strictly on the application of first principles of classical field theory. The practical relevance of the approach was then supported in simulations and in an established stable arrhythmia (atrial flutter), providing evidence of a technical advance. Reduction of far-field interference in CD-derived maps contributes a preferred method for the tracking of rapidly changing rhythms that ought to be ideally suited to mapping fibrillation. Second, the patterns of activation observed by CD consist of both re-entrant and focal activation that is patient specific and consistent with those obtained previously by others based on less specific voltage measurements (12, 16, 26, 44). In the earliest canine models of AF, the observed complex rhythms were described as “impure flutter” (58), indicating some level of organization. Today, there are abundant clinical observations to support re-entrant rotational (16, 26, 44, 45) and focal or co-existent mechanisms (12, 68). The cycle lengths observed at around 150 ms (6–8 Hz) are broadly in the range of those reported by others (11, 63, 69, 70), with the locations of principal drivers corresponding to those previously identified in contact (71) and noncontact studies (12). It is well established that pulmonary veins (72) and adjacent regions, particularly involving the posterior left atrial wall (11, 44, 63, 69), harbor important drivers in paroxysmal (72) and persistent AF (73) and are consistent with the results reported herein. Finally, relevant participation by identified drivers can only be fully imputed when delivery of therapy at the associated locations achieves normal rhythm and prevents arrhythmia re-induction (31, 74). In this report, a representative example of such a response in a patient with AF using CD-based activation maps to target ablation is illustrated. To address broader-scale impact of the methodology, a prospective clinical trial was designed and conducted to examine the effectiveness of CD mapping in identifying mechanisms that can be targeted for ablative treatment in persistent AF. Procedural intervention and follow-up is now complete in 127 treated individuals, with results reported separately.

The physiologic basis of the patterns reported remains to be established, but the assumption is that wavefronts interact along anatomical/functional barriers giving rise to rotational or fibrillatory conduction (13, 75). There are points of contention and several questions that have not been explored further in these studies. First, there is a substantial biophysical literature based on the rotor concept examining fibrillatory mechanisms through numerical simulations and in model systems using voltage-sensitive dyes (17, 76). This work is now supplemented by evidence for participation of rotors in human AF (16). Here, we refer to rotational activation, as we lack the experimental means to confirm the presence of rotors that have a specific meaning confined to a subset of functional re-entry characterized by a curved

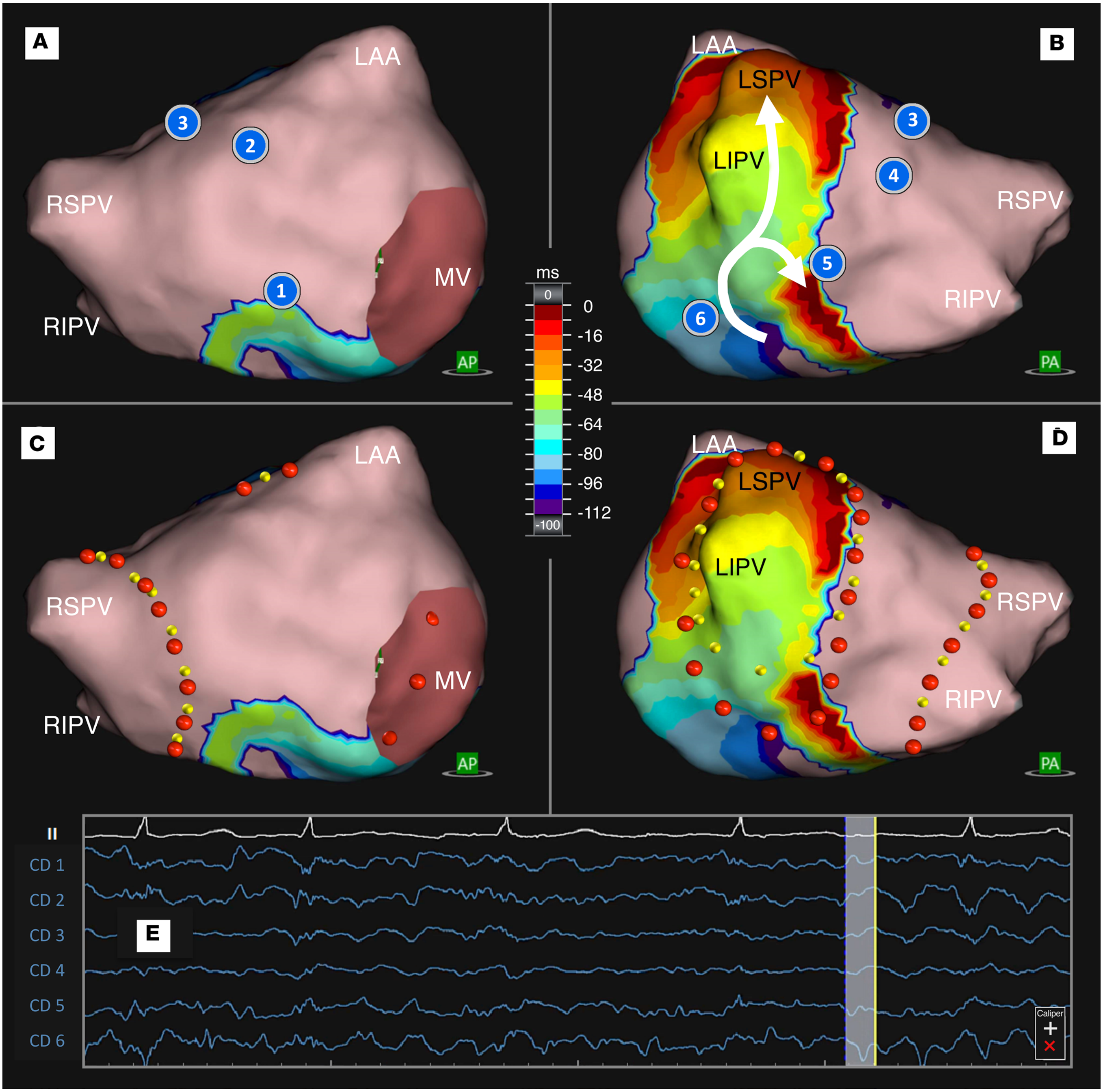

Figure 7. Case example of atrial fibrillation termination through targeted ablation. (**A**) Anterior-posterior (AP) view of left atrium with no classifiable activation patterns noted on anterior surface. (**B**) Posterior-anterior (PA) view of left atrium showing a single localized rotational activation (LRA) posterior and inferior to the left inferior pulmonary vein (LIPV). (**C**) Isolation of the right pulmonary veins (yellow dots) indicating the planned ablation line. No alterations, as indicated by the red dots, were made to the ablation line. (**D**) Incorporation of the LRA within the isolation line of the left pulmonary veins based on proximity of the central point of the LRA to the planned line that was altered to pass through the central point of the LRA. The yellow dots indicate the original planned line and the red dots the executed ablation line. While ablating within the identified area of interest, the AF terminated to sinus rhythm. The isolation line was completed, with block verified in sinus rhythm. (**E**) Calculated CD signals are displayed at locations 1-6 on the 3D anatomy displayed in panels **A** and **B**. The position of the yellow cursor, in time, correlates with the position of the leading edge of the red color band in the display of propagation history. CD signals 1–3 show predominantly positive (R-wave) unipolar CD morphology representing the resting state. CD signal number 4 shows a predominant QS morphology, with the yellow line crossing zero at the same instant that the red color band is reaching its location on the map. CD signal number 5 shows that depolarization occurred at that location at an earlier time in the propagation history. The duration of propagation history is displayed by the translucent-gray rectangle positioned behind the yellow time cursor and, in this example, the duration was set by the user to 112 ms (see Supplemental Videos 5 and 7).

wavefront and wavetail that meets at a non–refractory-phase singularity (60, 76). Second, the observations have been obtained exclusively from the anatomical surface mesh associated with the endocardium, with the role of the epicardium and endocardial-epicardial interactions (31, 68, 77) represented as a composite equivalent and thus not examined separately. Images of mid-myocardial or epicardial sources projected on the endocardial mesh at appropriate anatomical locations with associated signal morphologies correlated with myocardial depth. There is substantial evidence to implicate the 3D architecture of the atrial wall in the maintenance of AF with subendocardial bundles anchoring localized intramural re-entry. The responses to endocardial ablation obtained in the same human model are consistent with the responses reported and together support an independent importance for the endocardium (31). Third, the stability of actionable sites has not yet been formally addressed and repeated observations will be required to examine whether conduction patterns stabilize to specific locations over longer time scales (12, 45, 68). A subset of patients in the prospective study are being examined for consistency of identified localized sites that appear to drive or maintain AF over periods of time spanning the duration of procedures, with results to be reported separately.

CD mapping provides a source description of myocardial activation for the first time to our knowledge that enables a deeper comprehension of conduction mechanisms underlying complex arrhythmias and the potential for significant therapeutic benefit (78). The first clinical cases demonstrate that AF is a mappable arrhythmia with complex but repetitive patterns from which far-reaching implications are likely to emerge. Integration of accurate, patient-specific source determination with genomic, functional, and in silico analyses (79) strengthens the expectation of an improved understanding of the biology of the cardiac rhythm (80).

Methods

Study design. The objective of this evaluation of feasibility was to obtain unperturbed, high-resolution, global maps of the sources of cardiac activation during complex arrhythmias. Several steps were required to accomplish this objective: (a) proof that the approach achieved the predicted level of enhanced resolution (4, 81), through application of an established simulation model (24); (b) construction of instrumentation that provided real-time, noncontact electrical sensing and ultrasonic reconstruction of heart-chamber anatomy; and (c) development of a CD-based computational platform that reproduced both well-established and complex arrhythmias (atrial flutter and AF, respectively). The clinical studies are largely observational and were not blinded or randomized and sample sizes were based on previous study designs of novel approaches to the mapping of cardiac arrhythmias (26, 82). Examples of the responses to the delivery of ablation lesions are reported to support physiological relevance of activation patterns in the associated circuits, fulfilling a criterion for involvement established by Mines (74). No data have been excluded from the evaluation.

CD calculations. The mathematical derivation of the CD distribution has been covered in detail elsewhere (4, 81) (see also supplemental materials). Macroscopic electrostatics was applied to the blood-filled heart chamber with the accepted assumption that the electrical characteristics of blood are homogeneous and uniform (4). The heart itself was modeled as a uniform volume conductor with the myocardial wall represented as a 2D surface, S, that is defined by the endocardial boundary at any given instant of time. The depolarization and repolarization of the cardiac cell membrane was then represented as an equivalent, continuous distribution of CD formed by the sum of microscopic dipoles located within the 3D myocardium. The calculation of CD on the endocardial surface requires high-fidelity electrical input data, $V(\vec{x}, t)$, which were acquired using our purpose-built multi-electrode catheter (AcQMap) at various locations in the heart chamber. Distance measurements afforded by the ultrasound transducers account for errors that may otherwise arise from the motion of the heart, from the catheter, or from their interactions.

This source model allows for treating the problem as quasi-static, as cardiac activation propagates at a rate that is 10^8 times slower than the propagation of the electric field, which travels at the speed of light throughout the aqueous medium. As such, the cardiac field is not dependent on time and, in accordance with classical electrostatics and the application of Maxwell's equations, the calculation of potential or CD can be performed at any given instant using a solution to Poisson's equation, which relates the distribution of sources to the voltage within and surrounding the sources (4) (see also supplemental materials).

The voltage at any location on the endocardium can be separated into 2 components that represent the contribution from local sources and far-field sources:

$$V(\vec{x}_S) = -2\pi d(\vec{x}_S) + \int_S d(\vec{y})\,\frac{cos\varphi_{xy}}{|\vec{x}-\vec{y}|^2}\,d\sigma_y$$

Where $V(\vec{x}_S)$ is the voltage at any point on the endocardium, $-2\pi d(\vec{x}_S)$ represents the component of voltage contributed by local sources, and

$\int_S d(\vec{y})\,\frac{cos\varphi_{xy}}{|\vec{x}-\vec{y}|^2}\,d\sigma_y$ represents the component of voltage contributed by the sum of all surrounding and distant sources.

More generally, the voltage at any point within the chamber cavity and outside the chamber epicardium is entirely represented by the far-field component, as the local endocardial contributions are intrinsically included within the total distribution of sources that reside within the chamber myocardium. Accordingly, the voltage at any such point is expressed as:

$$V(\vec{x}) = \int_S d(\vec{y})\,\frac{cos\varphi_{xy}}{|\vec{x}-\vec{y}|^2}\,d\sigma_y$$

Where $V(\vec{x}_S)$ is the voltage at any point inside or outside the chamber myocardium, and

$\int_S d(\vec{y})\,\frac{cos\varphi_{xy}}{|\vec{x}-\vec{y}|^2}\,d\sigma_y$ represents voltage contributed by the sum of all sources residing within the myocardium.

Consequently, the algorithm consists of a transfer matrix that relates 48 points of measured voltage on the AcQMap catheter electrodes (left side of equation, known) to a discretized set of more than 3,600 equivalent local sources on the endocardial surface (right side of equation, unknown). The transfer matrix is regularized and inverted to obtain a high-density derivation of the separated, equivalent local sources on the endocardium, defined above as $-2\pi d(\vec{x}_S)$. This calculation represents the critical strategic advantage over conventional voltage-based mapping, with an unprecedented improvement in spatial resolution increasing from approximately 10 mm to 2.5 mm. Recalculating the CD, independently, at every measured sample time captures the temporal dynamics of propagation of CD across the surface of the chamber anatomy. The complete spatiotemporal embodiment of CD, $d(t, x)$ is thereby achieved, with the function of time represented parametrically.

Overall system description. The single-platform high-resolution imaging and mapping system employed provides heart chamber reconstruction using 3D ultrasound overlaid with high-resolution maps of electrical activation either as CD or voltage. The system is conceptually similar to conventional contact systems that combine 3D anatomical reconstruction and electrical signals (11, 26, 47). Cardiac voltage arises as a spatially broad summation of local charge sources generated by the action of cellular ion channels throughout the myocardium. CD (coulombs/cm) represents the magnitude of these sources, with a reduced contribution from far-field sources on the endocardial surface of the chamber and with a view of cardiac activity that is at least 4 times sharper and narrower than voltage (Figure 1). The system derives CD from noncontact sensing of cardiac unipolar potentials within the chamber cavity and localizes auxiliary catheters within and around the surface. The system also has a real-time graphical user interface (GUI) and supporting hardware for display of cardiac chamber anatomy and CD with respect to time (Figure 4A).

Catheter design, fabrication, and deployment. The diagnostic recording catheter (AcQMap 3D Imaging and Mapping Catheter) is a single-use device that has a 10-F nondeflectable shaft, an integral handle, and an expandable distal apparatus designed to yield a global examination of a cardiac chamber of interest and acquire data without the need to contact the chamber surface (noncontact mapping). The distal apparatus forms a 25-mm spheroid of 6 splines, each populated with 8 single-element ultrasound transducers and 8 low-impedance, high-fidelity, biopotential electrodes, with a total of 48 of each type of sensor (Figure 4B). The transducers provide distances between the splines and the endocardial surface. The electrodes are engineered for both a small size (~0.8 mm^2) and a low impedance to maximize signal-to-noise ratio, preserve baseline flatness, and maximize the fidelity for sensing the cardiac electric field. Body-surface ECG and patch electrodes are placed on the patient to provide ECG signals and localization data to the system. The catheter is deployed in the cardiac chamber of interest through a purpose-built deflectable introducer sheath over a 0.032-inch guidewire (Figure 4C) and ultrasound is activated to measure points of first reflection and reconstruct the endocardial anatomy. A respiration removal filter extracts low-frequency respiration signals from the EGMs and distance vectors. The catheter is connected to a computerized medical instrument (Figure 4A, console and workstation).

Ultrasound imaging. The combined operation of impedance localization of electrodes and ultrasound distance measurements provides the precise spatial relationship of the electrodes to the reconstructed endocardial surface required for the inverse solution. The endocardial surface is sampled by the ultrasound subsystem at a rate of up to 115,000 surface points per minute and the 3D surface is algorithmically reconstructed from the ultrasound point set in real time, with distance acquisition based on the transit time from transducer excitation to receipt of first sonic reflection. To scan the entire atrial surface anatomy, the catheter is slowly rotated within the deflectable guiding sheath, approximately 60 degrees clockwise and then counter-clockwise, while also advancing and retracting the catheter within the sheath throughout the chamber (Figure 4D and Supplemental Video 1). The measurement range of the 48 ultrasound transducers is approximately 7 cm. The reconstructed atrial chamber is a surface mesh composed of 3,648 vertices and 7,296 triangles (Figure 4D). Minimal editing is applied to achieve the final, CT-quality reconstructed anatomy, including removal of the mitral/tricuspid valve area. Navigation, mapping, and placement of ablation markers are performed directly within and upon the reconstructed atrial surface mesh.

Unipolar voltage data acquisition and analysis. Low-noise, high-fidelity biopotential amplifiers simultaneously acquire the 48 raw, noncontact, unipolar intracavitary voltage samples at a collective rate of exactly 150,000 per second. The amplifiers are designed to maximize the signal-to-noise ratio, minimize filter distortion, and to preserve baseline flatness. The spatial distribution of these samples is sufficient to achieve global mapping of cardiac activity over any selected duration of time and independent of the stability of the rhythm. All recordings from the noncontact catheter were 30 seconds in duration. Inverse and forward algorithms were applied to the intracardiac voltage to derive and display 3D maps of unipolar CD and voltage, respectively (Figure 1D and Supplemental Video 2). Processing of CD maps occurs within seconds, enabling immediate identification of actionable therapy targets and allowing for rapid, iterative mapping to assess the effect of treatment. The calculated data are spatially and temporally applied to the final processed surface anatomy and presented statically or dynamically as either a depolarization map or propagation-history map. Maps of regular rhythms were calculated for as many integer multiples of the arrhythmia cycle length obtainable between the end of a T wave and the subsequent QRS complex. Maps of AF were calculated for durations ranging from 5 to 10 seconds. The area of depolarization is shown on the map in Figure 1C at a specific instant of time, with the red region depicting the negative phase of CD, both as an area spanning space and as an associated unipolar waveform through time. As shown, the negative phase is correlated with phase 2 of the action potential. Animation of subsequent map instants reveals propagation of depolarization. In the propagation history maps (Figures 5–7, and Supplemental Videos 2–7), the red color band represents the leading edge of the activation wavefront at a present fiducial instant of time (t_0 = 0 ms), with the trailing color bands showing earlier locations of the wavefront in equal steps backward in time. Concurrently, the zero instant is marked by the yellow time cursor in the waveform window and the gray rectangle represents the total duration of time spanned by the color bands. The history window is adjustable by the user and is generally set at 75% of the arrhythmia cycle length. When animated, the color bands portray a contiguous flow from the newest instant (red) to the oldest instant (purple) that enables intuitive comprehension of the global pattern of propagation for every activation cycle in both regular and irregular arrhythmias. Ultimately, in this and all modes of color maps, red represents the key element to be focused on, such as (a) the leading edge of the wavefront in an animated propagation-history map, (b) the site of early activation in a fixed isochronal map, and (c) the location of lowest amplitude in a voltage map.

Study cohort and clinical studies. Patients aged 18–75 years diagnosed with atrial arrhythmias and scheduled for ablation were eligible for enrollment in the DDRAMATIC SVT trial (NCT01875614) (83). In patients with AF, the protocol required application of a present-day 3D mapping system to guide the established treatment approach for isolation of the pulmonary veins, followed by additional targeted ablation guided by the new imaging and mapping system. This approach allowed comparison against the current gold standards (84). The subsets of patients included in this report were recruited at 3 of the participating centers. Diagnosis of atrial flutter was based on established clinical and electrocardiographic features (25, 27) and persistent AF was conventionally defined as AF that had lasted more than 7 days without self-termination (12). Patients on antiarrhythmic agents had these withheld for more than 5 half-lives, with none having any recent exposure to amiodarone. Each patient had undergone prior CT imaging of the LA, pulmonary veins, and their junctions.

Procedures were conducted under either general anesthesia or conscious sedation and mapping catheters were advanced transvenously to the heart from both right and left femoral veins. Positioning in the RA was achieved directly and in the LA following trans-septal needle access across the interatrial septum (Figure 4C). Heparin was administered, maintaining activated clotting time greater than 350 seconds prior to deployment of the AcQMap catheter in left atria. In addition, unipolar and positional reference catheters were placed in the inferior vena cava and azygos vein, respectively. Concurrently, the mapping system evolved so that in later procedures an internal position reference (azygos vein) was no longer required. Regions of interest were identified with areas targeted for radiofrequency ablation receiving contiguous lesions connected to electrically inert boundaries followed by remapping through reacquisition of noncontact EGMs.

Statistics. Statistical analysis was performed for normally distributed data using a 2-sided, unpaired *t* test for comparing between 2 groups, with an α level of 0.05. A 1-way ANOVA with a Tukey's post hoc test was used for groups of more than 2, with an α level of 0.05. For data that were not normally distributed, a Mann-Whitney nonparametric test was used to compare between 2 groups. Data are presented as means ± SD or median and IQR (Q1–Q3). *P* less than 0.08 was considered significant.

Study approval. The clinical procedures were conducted according to the Declaration of the Helsinki principles and approved by all relevant Institutional Review Boards in Cambridge, Hamburg, and Toronto, with all patients participating providing written, informed consent.

Author contributions

GS and LD were responsible for the design of mathematical models and the prototype algorithm. MZ, XS, DC, and GB completed the computational model and developed the algorithm, and designed the control system and software for inclusion in the console and the clinical recordings. AG, SW, CM, AV, and PH completed the clinical studies. DC and GB fabricated the catheter, console, and control systems. AG, SW, AV, CS, and GB designed the research. AG, SW, AV, DC, and GB analyzed the data. AG, MZ, XS, and GB wrote the manuscript. All authors approved the final version of the manuscript.

Acknowledgments

We are particularly grateful to Janice Barstad for assistance in the preparation of illustrations and the curation of the data files. We are also grateful to Nathan Angel and Pratik Shah for generation of simulation data. The National Institute for Health Research (NIHR) Translational Research Program at Royal Papworth Hospital and Acutus Medical supported the study.

Address correspondence to: Andrew Grace, Department of Biochemistry, University of Cambridge, Hopkins Building, Tennis Court Road, Cambridge CB2 1QW, United Kingdom. Phone: 44.7767.420.465; Email: aag1000@cam.ac.uk.

---

1. De Ambroggi L, Taccardi B. Current and potential fields generated by two dipoles. *Circ Res*. 1970;27(6):901–911.
2. Geselowitz DB. Electric and magnetic field of the heart. *Annu Rev Biophys Bioeng*. 1973;2:37–64.
3. Plonsey R, van Oosterom A. Implications of macroscopic source strength on cardiac cellular activation models. *J Electrocardiol*. 1991;24(2):99–112.
4. Scharf G, Dang L. Dipole density instead of potentials in electrocardiology. Cornell University. http://arxiv.org/pdf/1601.04419v1.pdf. Published January 18, 2016. Accessed February 20, 2019.
5. Waller AD. A Demonstration on man of electromotive changes accompanying the heart's beat. *J Physiol (Lond)*. 1887;8(5):229–234.
6. Wilson FN, Macleod AG, Barker PS. The distribution of the action currents produced by heart muscle and other excitable tissues immersed in extensive conducting media. *J Gen Physiol*. 1933;16(3):423–456.
7. Wilson FN, Johnston FD. On Einthoven's triangle, the theory of unipolar electrocardiographic leads, and the interpretation of the precordial electrocardiogram. *Am Heart J*. 1946;32:277–310.
8. Macfarlane PWE, Lawrie TDV. *Comprehensive Electrocardiology: Theory and Practice in Health and Disease*. Vols 1–3. Oxford, UK: Pergamon Press; 1989.
9. Stevenson WG, Soejima K. Recording techniques for clinical electrophysiology. *J Cardiovasc Electrophysiol*. 2005;16(9):1017–1022.
10. de Bakker JM, Wittkampf FH. The pathophysiologic basis of fractionated and complex electrograms and the impact of recording techniques on their detection and interpretation. *Circ Arrhythm Electrophysiol*. 2010;3(2):204–213.
11. Atienza F, et al. Comparison of radiofrequency catheter ablation of drivers and circumferential pulmonary vein isolation in atrial fibrillation: a noninferiority randomized multicenter RADAR-AF trial. *J Am Coll Cardiol*. 2014;64(23):2455–2467.

12. Haissaguerre M, et al. Driver domains in persistent atrial fibrillation. *Circulation*. 2014;130(7):530–538.
13. Nattel S, Dobrev D. Controversies about atrial fibrillation mechanisms: Aiming for order in chaos and whether it matters. *Circ Res*. 2017;120(9):1396–1398.
14. Verma A, et al. Approaches to catheter ablation for persistent atrial fibrillation. *N Engl J Med*. 2015;372(19):1812–1822.
15. Calkins H. The dynamic substrate for atrial fibrillation: Can we identify it and is it of clinical importance? *JACC Clin Electrophysiol*. 2017;3(4):403–404.
16. Narayan SM, Krummen DE, Shivkumar K, Clopton P, Rappel WJ, Miller JM. Treatment of atrial fibrillation by the ablation of localized sources: CONFIRM (Conventional Ablation for Atrial Fibrillation With or Without Focal Impulse and Rotor Modulation) trial. *J Am Coll Cardiol*. 2012;60(7):628–636.
17. Nattel S, Xiong F, Aguilar M. Demystifying rotors and their place in clinical translation of atrial fibrillation mechanisms. *Nat Rev Cardiol*. 2017;14(9):509–520.
18. Schilling RJ, Peters NS, Davies DW. Simultaneous endocardial mapping in the human left ventricle using a noncontact catheter: comparison of contact and reconstructed electrograms during sinus rhythm. *Circulation*. 1998;98(9):887–898.
19. Abrams DJ, et al. Comparison of noncontact and electroanatomic mapping to identify scar and arrhythmia late after the Fontan procedure. *Circulation*. 2007;115(13):1738–1746.
20. Helmholtz H. Ueber einige Gesetze der Vertheilung elektrischer Ströme in körperlichen Leitern mit Anwendung auf die thierisch-elektrischen Versuche. *Ann Phys*. 1853;89(6):211–233.
21. Scharf G. *From electrostatics to optics: a concise electrodynamics course*. London, UK: Springer-Verlag Berlin; 1994.
22. Zangwill A. *Modern electrodynamics*. Cambridge, UK: Cambridge University Press; 2013.
23. Tikhonov AN, Arsenin VI. *Solutions of ill-posed problems*. Washington, D.C.: John Wiley & Sons; 1977.
24. Mirams GR, et al. Chaste: an open source C++ library for computational physiology and biology. *PLoS Comput Biol*. 2013;9(3):e1002970.
25. Schilling RJ, Peters NS, Goldberger J, Kadish AH, Davies DW. Characterization of the anatomy and conduction velocities of the human right atrial flutter circuit determined by noncontact mapping. *J Am Coll Cardiol*. 2001;38(2):385–393.
26. Daoud EG, et al. Identification of repetitive activation patterns using novel computational analysis of multielectrode recordings during atrial fibrillation and flutter in humans. *JACC Clin Electrophysiol*. 2017;3(3):207–216.
27. Pathik B, et al. New insights into an old arrhythmia: High-resolution mapping demonstrates conduction and substrate variability in right atrial macro-re-entrant tachycardia. *JACC Clin Electrophysiol*. 2017;3(9):971–986.
28. Gaspo R, Bosch RF, Talajic M, Nattel S. Functional mechanisms underlying tachycardia-induced sustained atrial fibrillation in a chronic dog model. *Circulation*. 1997;96(11):4027–4035.
29. Hang S. TetGen, a Delaunay-Based Quality Tetrahedral Mesh Generator. ACM Transactions on Mathematical Software (TOMS). 2015;41(2): https://doi.org/10.1145%2F2629697.
30. Earley MJ, Abrams DJ, Sporton SC, Schilling RJ. Validation of the noncontact mapping system in the left atrium during permanent atrial fibrillation and sinus rhythm. *J Am Coll Cardiol*. 2006;48(3):485–491.
31. Hansen BJ, et al. Atrial fibrillation driven by micro-anatomic intramural re-entry revealed by simultaneous sub-epicardial and sub-endocardial optical mapping in explanted human hearts. *Eur Heart J*. 2015;36(35):2390–2401.
32. Hecht HH. Some observations and theories concerning the electrical behavior of heart muscle. *Am J Med*. 1961;30:720–746.
33. Plonsey R. Volume conductor fields of action currents. *Biophys J*. 1964;4:317–328.
34. Panofsky WKH, Phillips MN. *Classical Electricity and Magnetism.* 2nd ed. Reading, MA: Addison-Wesley Publishing Co.; 1962.
35. van Oosterom A. Solidifying the solid angle. *J Electrocardiol*. 2002;35 Suppl:181–192.
36. Plonsey R. The nature of sources of bioelectric and biomagnetic fields. *Biophys J*. 1982;39(3):309–312.
37. Craib WH. The Electrocardiogram. An investigation of the principles underlying the interpretation of the electrical responses of muscle nerve, with special reference to the electrocardiogram. Medical Research Council: Oxford University Press; 1930. Special Report Series No. 147. London: HMSO.
38. Qu Z, Weiss JN. Mechanisms of ventricular arrhythmias: from molecular fluctuations to electrical turbulence. *Annu Rev Physiol*. 2015;77:29–55.
39. Hodgkin AL, Huxley AF. A quantitative description of membrane current and its application to conduction and excitation in nerve. *J Physiol (Lond)*. 1952;117(4):500–544.
40. Corbin LV, Scher AM. The canine heart as an electrocardiographic generator. Dependence on cardiac cell orientation. *Circ Res*. 1977;41(1):58–67.
41. Jackson JD. *Classical electrodynamics*. New York, NY; Wiley; 1999.
42. Bear LR, et al. How accurate is inverse electrocardiographic mapping? A systematic in vivo evaluation. *Circ Arrhythm Electrophysiol*. 2018;11(5):e006108.
43. Rudy Y. The forward problem of electrocardiography revisited. *Circ Arrhythm Electrophysiol*. 2015;8(3):526–528.
44. Cluitmans MJM, et al. In vivo validation of electrocardiographic imaging. *JACC Clin Electrophysiol*. 2017;3(3):232–242.
45. Haissaguerre M, et al. Intermittent drivers anchoring to structural heterogeneities as a major pathophysiological mechanism of human persistent atrial fibrillation. *J Physiol (Lond)*. 2016;594(9):2387–2398.
46. Zahid S, et al. Patient-derived models link re-entrant driver localization in atrial fibrillation to fibrosis spatial pattern. *Cardiovasc Res*. 2016;110(3):443–454.
47. Roney CH, et al. Spatial resolution requirements for accurate identification of drivers of atrial fibrillation. *Circ Arrhythm Electrophysiol*. 2017;10(5):e004899.
48. Nakagawa H, Ikeda A, Sharma T, Lazzara R, Jackman WM. Rapid high resolution electroanatomical mapping: evaluation of a new system in a canine atrial linear lesion model. *Circ Arrhythm Electrophysiol*. 2012;5(2):417–424.
49. Laughner J, et al. Practical considerations of mapping persistent atrial fibrillation with whole-chamber basket catheters. *JACC Clin Electrophysiol*. 2016;2(1):55–65.
50. Taccardi B, Arisi G, Macchi E, Baruffi S, Spaggiari S. A new intracavitary probe for detecting the site of origin of ectopic ventricular beats during one cardiac cycle. *Circulation*. 1987;75(1):272–281.
51. Kadish A, Hauck J, Pederson B, Beatty G, Gornick C. Mapping of atrial activation with a noncontact, multielectrode catheter

in dogs. *Circulation*. 1999;99(14):1906–1913.
52. Gornick CC, Adler SW, Pederson B, Hauck J, Budd J, Schweitzer J. Validation of a new noncontact catheter system for electroanatomic mapping of left ventricular endocardium. *Circulation*. 1999;99(6):829–835.
53. Khoury DS, Rudy Y. A model study of volume conductor effects on endocardial and intracavitary potentials. *Circ Res*. 1992;71(3):511–525.
54. Khoury DS, Taccardi B, Lux RL, Ershler PR, Rudy Y. Reconstruction of endocardial potentials and activation sequences from intracavitary probe measurements. Localization of pacing sites and effects of myocardial structure. *Circulation*. 1995;91(3):845–863.
55. Bun SS, Latcu DG, Marchlinski F, Saoudi N. Atrial flutter: more than just one of a kind. *Eur Heart J*. 2015;36(35):2356–2363.
56. Nattel S. New ideas about atrial fibrillation 50 years on. *Nature*. 2002;415(6868):219–226.
57. Skanes AC, Mandapati R, Berenfeld O, Davidenko JM, Jalife J. Spatiotemporal periodicity during atrial fibrillation in the isolated sheep heart. *Circulation*. 1998;98(12):1236–1248.
58. Lewis T. *The Mechanism and Graphic Registration of the Heart Beat*. 3rd ed. London, UK; Shaw & Sons: 1925.
59. Schuessler RB, Grayson TM, Bromberg BI, Cox JL, Boineau JP. Cholinergically mediated tachyarrhythmias induced by a single extrastimulus in the isolated canine right atrium. *Circ Res*. 1992;71(5):1254–1267.
60. Gray RA, Pertsov AM, Jalife J. Spatial and temporal organization during cardiac fibrillation. *Nature*. 1998;392(6671):75–78.
61. Botteron GW, Smith JM. Quantitative assessment of the spatial organization of atrial fibrillation in the intact human heart. *Circulation*. 1996;93(3):513–518.
62. Gerstenfeld EP, Sahakian AV, Swiryn S. Evidence for transient linking of atrial excitation during atrial fibrillation in humans. *Circulation*. 1992;86(2):375–382.
63. Sanders P, et al. Spectral analysis identifies sites of high-frequency activity maintaining atrial fibrillation in humans. *Circulation*. 2005;112(6):789–797.
64. Zaman JAB, et al. Identification and characterization of sites where persistent atrial fibrillation is terminated by localized ablation. *Circ Arrhythm Electrophysiol*. 2018;11(1):e005258.
65. Scharf C, et al. Acute effects of left atrial radiofrequency ablation on atrial fibrillation. *J Cardiovasc Electrophysiol*. 2004;15(5):515–521.
66. Narayan SM, Jalife J. CrossTalk proposal: Rotors have been demonstrated to drive human atrial fibrillation. *J Physiol (Lond)*. 2014;592(15):3163–3166.
67. Allessie M, de Groot N. CrossTalk opposing view: Rotors have not been demonstrated to be the drivers of atrial fibrillation. *J Physiol (Lond)*. 2014;592(15):3167–3170.
68. Lee G, et al. Epicardial wave mapping in human long-lasting persistent atrial fibrillation: transient rotational circuits, complex wavefronts, and disorganized activity. *Eur Heart J*. 2014;35(2):86–97.
69. Lazar S, Dixit S, Marchlinski FE, Callans DJ, Gerstenfeld EP. Presence of left-to-right atrial frequency gradient in paroxysmal but not persistent atrial fibrillation in humans. *Circulation*. 2004;110(20):3181–3186.
70. Vogler J, et al. Pulmonary vein isolation versus defragmentation: The CHASE-AF clinical trial. *J Am Coll Cardiol*. 2015;66(24):2743–2752.
71. Seitz J, et al. AF ablation guided by spatiotemporal electrogram dispersion without pulmonary vein isolation: A wholly patient-tailored approach. *J Am Coll Cardiol*. 2017;69(3):303–321.
72. Haïssaguerre M, et al. Spontaneous initiation of atrial fibrillation by ectopic beats originating in the pulmonary veins. *N Engl J Med*. 1998;339(10):659–666.
73. Santangeli P, et al. Prevalence and distribution of focal triggers in persistent and long-standing persistent atrial fibrillation. *Heart Rhythm*. 2016;13(2):374–382.
74. Mines GR. On circulating excitations in heart muscle and their possible relation to tachycardia and fibrillation. *Trans R Soc Canada*. 1914;(4):43–52.
75. Berenfeld O, Zaitsev AV, Mironov SF, Pertsov AM, Jalife J. Frequency-dependent breakdown of wave propagation into fibrillatory conduction across the pectinate muscle network in the isolated sheep right atrium. *Circ Res*. 2002;90(11):1173–1180.
76. Pandit SV, Jalife J. Rotors and the dynamics of cardiac fibrillation. *Circ Res*. 2013;112(5):849–862.
77. de Groot N, et al. Direct proof of endo-epicardial asynchrony of the atrial wall during atrial fibrillation in humans. *Circ Arrhythm Electrophysiol*. 2016;9(5):e003648.
78. Marrouche NF, et al. Catheter ablation for atrial fibrillation with heart failure. *N Engl J Med*. 2018;378(5):417–427.
79. Schafer S, et al. Titin-truncating variants affect heart function in disease cohorts and the general population. *Nat Genet*. 2017;49(1):46–53.
80. Grace AA, Roden DM. Systems biology and cardiac arrhythmias. *Lancet*. 2012;380(9852):1498–1508.
81. Scharf G, Dang L, Scharf C. Electrophysiology of living organs from first principles. Cornell University. http://arxiv.org/PS_cache/arxiv/pdf/1006/1006.3453v1.pdf. Published June 17, 2010. Accessed February 20, 2019.
82. Wang Y, et al. Noninvasive electroanatomic mapping of human ventricular arrhythmias with electrocardiographic imaging. *Sci Transl Med*. 2011;3(98):98ra84.
83. Bittner A. Dipole density mapping in supraventricular tachycardia (DDRAMATIC-SVT). NIH. https://clinicaltrials.gov/ct2/show/NCT01875614. Published June 11, 2015. Updated January 30, 2019. Accessed February 20, 2019.
84. Kuck KH, et al. Impact of complete versus incomplete circumferential lines around the pulmonary veins during catheter ablation of paroxysmal atrial fibrillation: results from the Gap-Atrial Fibrillation-German Atrial Fibrillation Competence Network 1 Trial. *Circ Arrhythm Electrophysiol*. 2016;9(1):e003337.